

Infrared radiative transfer modelling in a 3D scattering cloudy atmosphere: Application to limb sounding measurements of cirrus

G.B.L. Ewen^{a,*}, R.G. Grainger^a, A. Lambert^b, A.J. Baran^c

^a*Department of Atmospheric, Oceanic and Planetary Physics, University of Oxford, Clarendon Laboratory, Parks Road, Oxford, OX1 3PU, UK*

^b*National Center for Atmospheric Research (NCAR), Boulder, CO, USA*

^c*Met Office, Exeter, UK*

Received 16 October 2004; accepted 23 December 2004

Abstract

The Monte Carlo cloud scattering forward model (McClouds_FM) has been developed to simulate limb radiative transfer in the presence of cirrus clouds, for the purposes of simulating cloud contaminated measurements made by an infrared limb sounding instrument, e.g. the Michelson Interferometer for Passive Atmospheric Sounding (MIPAS). A *reverse* method three-dimensional Monte Carlo transfer model is combined with a line-by-line model for radiative transfer through the non-cloudy atmosphere to explicitly account for the effects of multiple scattering by the clouds. The ice cloud microphysics are characterised by a size distribution of randomly oriented ice crystals, with the single scattering properties of the distribution determined by accurate calculations accounting for non-spherical habit.

A comparison of McClouds_FM simulations and real MIPAS spectra of cirrus shows good agreement. Of particular interest are several noticeable spectral features (i.e. H₂O absorption lines) in the data that are replicated in the simulations: these can only be explained by upwelling tropospheric radiation scattered into the line-of-sight by the cloud ice particles.

© 2005 Elsevier Ltd. All rights reserved.

Keywords: Limb radiative transfer; Cirrus; Multiple scattering; Monte Carlo

*Corresponding author. Tel.: +44 1865 272912; fax: +44 1865 272923.

E-mail address: gewen@atm.ox.ac.uk (G.B.L. Ewen).

1. Introduction

It is now well known that cirrus permanently covers about 30% of the Earth's surface [1] and that high level cirrus clouds have a particularly strong influence on Earth's radiation budget [2]. The current state of knowledge concerning cirrus radiative properties is not yet sufficiently complete to allow a comprehensive description of how cirrus effects the global radiation balance. In most instances the determination of cirrus properties over such large spatial and temporal scales requires the use of satellite data. The radiative effects of cirrus are governed to a large extent by their physical and microphysical properties [3] and it follows that most satellite data studies of cirrus concentrate on inferring these properties and obtaining global distributions.

There are many different techniques for determining cirrus properties from passive satellite observations. Predominantly, these techniques focus on a limited number of parameters to quantify cirrus clouds. These include the spatial coverage, top and base altitude, top and base temperatures, optical thickness, vertical ice water path and the effective particle size and shape. With respect to measuring optically thin cloud, limb observations have a greater inherent detection sensitivity compared to nadir observations [4–6] due to the small elevation angle clouds are viewed at, which maximizes their opacity. Both the Stratospheric Aerosol and Gas Experiment (SAGE) II and the HALogen Occultation Experiment (HALOE) instruments have demonstrated the detection sensitivity of limb sounders to tenuously thin (known as subvisible) cirrus [7,8]. This cirrus occurs mostly in the upper troposphere in the tropics, and is not only radiatively important [9], but also plays an important role in the dehydration of air entering the tropical lower stratosphere [10].

Predominantly, limb sounders that have been used to obtain information on tenuous cirrus clouds have been occultation instruments, e.g. SAGE-II, HALOE, Atmospheric Trace MOlecule Spectroscopy (ATMOS) [11–13]. However, Mergenthaler et al. [14] and Spang et al. [15] have demonstrated that cirrus features are frequently observed by infrared emission instruments. Occultation instruments can detect subvisible cirrus as regions of enhanced extinction near the tropopause which do not obscure the solar beam. When opaque clouds are present the solar beam will be blocked in the occultation view, whereas the thermal emission measurement will generally observe more radiation. Thus, the thermal emission technique potentially has greater sensitivity for differentiating between cloud optical depth than the occultation technique.

Mergenthaler et al. [14], using the Cryogenic Limb Array Etalon Spectrometer (CLAES) emission measurements, noted that scattering of upwelling thermal radiation into the CLAES line-of-sight could significantly enhance the CLAES ability to detect cirrus. It was estimated that the radiation emanating toward CLAES from an ice cloud could be enhanced by 25% or more by scattering. The development of high fidelity space pointing limb sounders such as the Michelson Interferometer for Passive Atmospheric Sounding (MIPAS) and the HIGH Resolution Dynamic Limb Sounder (HIRDLS) presents an opportunity to further investigate the sensitivity of the limb thermal emission technique with greater global coverage than previous emission instruments. Observations of optically thin cloud made by both MIPAS and HIRDLS will measure radiation emitted from the cloud and also a radiance component which is transmitted from below the cloud due to scattering from cloud particles. In the case of the MIPAS measurements the tropospheric radiation scattered into the line-of-sight causes additional (absorption) structure in the spectra. Early studies of MIPAS data have demonstrated this for both Polar Stratospheric Clouds (PSCs)

[16] and for cirrus [17]. As scattering is dependent on cloud microphysics, this effect can give information about the microphysical properties of the scattering particles comprising the cloud.

In order to determine cloud properties from limb emission measurements the first requirement is a radiative transfer model to simulate the scattering of atmospheric thermal radiation by cirrus clouds. Such a model must be able to model spherical geometry and multiple-scattering radiance. Accurate radiative transfer models which satisfy these requirements for simulation of infrared limb emission spectra at high spectral resolution are not yet publicly available. Recent studies on limb emission measurements have relied on simpler calculations to model the scattering features caused by cloud. Spang et al. [17] investigated the effect of adding an arbitrary 10% radiance contribution of a nadir spectrum to a line-by-line calculated limb spectrum. They found similar spectral features in their model spectra compared to observations by MIPAS but the continuum signal was matched poorly with discrepancies of up to 40%. The more rigorous study by Höpfner [18] on modelling the effects of PSCs on limb spectra included Mie single scattering into a forward line-by-line code. The method was successful in modelling scattering features similar to those observed in MIPAS balloon spectra of PSCs [16], but encountered difficulty matching the baseline continuum signal.

The Monte Carlo Cloud scattering Forward Model (McClouds_FM) has been developed to accurately model infrared limb emission measurements of cirrus clouds, inclusive of multiple-scattering, spherical geometry and accurate cloud ice particle scattering properties. McClouds_FM will be a valuable tool in improving the understanding of the role played by multiple scattering in the analysis of limb measurements of cirrus. In addition, it is particularly powerful as it will be able to model high resolution infrared spectral limb measurements. The goal of McClouds_FM is that it will be able to replicate such limb measurements, e.g. from MIPAS, to within instrument noise and model error. Nominally, McClouds_FM should be able to reproduce limb measurements to within 5% of the continuum baseline level and spectral average.

Section 2 of this paper introduces McClouds_FM and describes the calculations used to simulate the radiance arriving at a limb sounder. Section 3 describes further considerations to simulate MIPAS data specifically. Section 4 presents a comparison of McClouds_FM results to real MIPAS data.

2. The forward model

The forward model, \mathbf{F} , used to calculate synthesised radiances at the satellite, $\hat{\mathbf{y}}$, can be represented by

$$\hat{\mathbf{y}} = \mathbf{F}(\hat{\mathbf{x}}_c, \hat{\mathbf{b}}), \quad (1)$$

where $\hat{\mathbf{x}}_c$ and $\hat{\mathbf{b}}$ are the best estimates of the cloud and atmosphere parameters. The vector $\hat{\mathbf{x}}_c$ is known as the state vector and contains all parameters necessary to characterise the cloud field: cloud particle effective radius, total number density of cloud particles, cloud top height and vertical depth of the cloud layer. The vector $\hat{\mathbf{b}}$ is the set of parameters required to characterise the atmosphere: these are critical to the resultant synthesised radiance but are chosen not to be included in the state vector (e.g. molecular cross sections).

The forward model must combine an estimate of the atmospheric radiance with the physics of the measurement. McClouds_FM breaks the problem down into two steps: computing the radiative transfer through the atmosphere, then modulating the radiance to take into account the effects of the observing instrument e.g. by modelling the field-of-view. In cloudy atmospheres, scattering and molecular absorption are involved in the radiative transfer which makes the physics of the forward function very complex. McClouds_FM splits the radiative transfer calculations into two regimes. The model is separated into a scattering domain, i.e. the cloud volume, and a non-scattering domain, i.e. the clear sky. In the clear sky domain line-by-line radiative transfer is used to calculate the emission and transmission along the ray paths. In the cloud domain a Monte Carlo *reverse* scattering model is used to simulate photon trajectories from a pencil beam from the detector arriving at the cloud in the backward direction. Effectively, McClouds_FM uses Monte Carlo radiative transfer to trace all photon ray paths backwards from the satellite then calculates the reciprocal radiative transfer along each path to determine the total radiance arriving at the detector.

2.1. Assumptions

This section outlines the basic assumptions made in order to simplify the radiative behaviour of the cloud-atmosphere system and to limit the number of parameters required to quantify the cloud in the model. The main consideration when making these assumptions is to preserve accuracy while making the forward model fast enough so that it can be used to retrieve cloud properties from limb emission observations.

2.1.1. Microphysical and single scattering properties

Cirrus clouds are composed principally of ice crystals with various non-spherical shapes. The sizes of the ice crystals can range from less than $10\ \mu\text{m}$ to about $4000\ \mu\text{m}$ [19], and the typical geometry of the crystals can range from single pristine shapes such as hexagonal ice columns or plates, to complex aggregates of columns or bullets [20]. There are many different definitions of cirrus, but for the purposes of this model cirrus clouds are considered to be composed entirely of (randomly oriented) non-spherical ice crystals and to occur at high altitudes, usually in the region of 70–80% of the tropopause level. In addition, the cirrus is assumed to be homogeneous, i.e. the cloud is composed of a single crystal habit, the cloud is spatially contiguous, and that there exists a size distribution which is representative of the entire cloud volume.

A single crystal habit is assumed in order to limit the degrees of freedom for the retrieved solution in the measurement inversion and to reduce the complexity and computation time of the scattering calculations in the forward model. There is a wealth of evidence from in situ aircraft measurements showing that cirrus with relatively small particle sizes (i.e. $< 150\ \mu\text{m}$) are frequently observed to have a dominating crystal habit [21]. Additionally, it is common for single-view instruments (such as The MODERate Resolution Imaging Spectrometer (MODIS)) to make some assumption about crystal shape in their retrieval of cirrus properties (e.g. [22]).

As McClouds_FM incorporates multiple scattering effects it is important to have accurate single scattering properties for the cloud particles. The use of the correct ice crystal scattering properties is key to reducing errors during the retrieval of optical thickness or microphysical properties of cirrus from remote measurements [22,23]. Due to the non-sphericity of ice crystals,

the theoretical description of their single-scattering properties is far more complicated than for their spherical counterparts. The single scattering properties used in McClouds_FM are the extinction coefficient, β_{ext} , single-scatter albedo, ω_0 , asymmetry parameter, g , and the scattering phase function. Therefore, McClouds_FM is flexibly configured to use any non-spherical crystal shape assuming that the single scattering properties input are accurately calculated.

In this paper hexagonal columns are assumed since for subvisual and non-convective laminar layer cirrus it is likely that such cloud consists of small pristine faceted ice crystals of less than 100 μm . For such small ice crystals there is no current evidence to suggest that these are not hexagonal. In addition hexagonal columns are a basic constituent of cirrus ice crystals and have been shown to reproduce certain well-known cirrus optical phenomena [24].

The single scattering properties used for hexagonal columns are calculated as in [25] for wavelengths between 5 and 16 μm and single particles of maximum dimensions ranging from 3.0 to 3500 μm . T-matrix methods (due to [26] and [27]) are applied to hexagonal columns to calculate total optical properties (i.e. β_{ext} , ω_0 and g) and phase functions for maximum dimensions up to about 40 μm . For sizes from 40 μm to about 175 μm T-matrix methods were applied to the equal area circular cylinder to compute the optical properties and phase function. Then finally the T-matrix electromagnetic solutions are supplemented for maximum dimensions greater than about 175 μm by the complex angular momentum (CAM) approximation. The CAM method is used to calculate the total optical properties but cannot be used to calculate the phase function, which has been calculated using a piecewise linear extension of the Henyey-Greenstein phase function due to [28].

The single scattering properties for the varying sizes of individual crystals are integrated over cirrus size distributions derived from in situ measurements [29] to give the bulk cloud scattering properties. The size distributions are described by the effective radius, r_e , and the total number density, N (i.e. the total number of cloud particles per unit volume). In order to avoid ambiguity in the meaning of an effective dimension for a cloud composed of ice crystals, the definition of effective radius r_e used in this paper will be

$$r_e = \frac{3}{4} \frac{\text{IWC}}{\rho \sum n_j A_j} \quad (2)$$

as given by Francis et al. [30], where IWC is the ice water content (mass per unit volume), n_j is the crystal concentration in the j th size bin, and A_j is the mean cross-sectional area of this bin, and ρ is a reference density of 1 g cm^{-3} .

The total number density is defined as

$$N = \int_0^\infty n(L) dL \simeq \sum n_j, \quad (3)$$

where L is the maximum particle dimension. The IWC can be expressed as

$$\text{IWC} = \rho_{\text{ice}} \sum n_j V_j, \quad (4)$$

where V_j is the mean volume of a crystal in the j th size bin and ρ_{ice} is the density of ice.

If the size distribution is normalised to a different total number density, the effective radius, single scatter albedo, asymmetry parameter and phase function are unchanged. However, the extinction coefficient and the IWC change by a factor equal to the ratio of the new number density

compared to the original. At a given wavelength the bulk single scattering properties for a cirrus cloud are characterised by the crystal habit, the effective radius of the polydispersion of cloud ice particles and the total number density.

2.1.2. Cloud geometry

The cloud geometry is approximated as a uniform depth spherical shell layer in the atmosphere, with a finite extent given by the angle ψ that the cloud edge subtends at the centre of the Earth. The geometry is then defined by the cloud top height, C_{top} (measured radially from the Earth's surface) and the vertical (radial) depth of the cloud layer, C_{depth} . The cloud volume is perhaps best described in Earth centred spherical coordinates as the locus of points $\{(r, \phi, \theta)\}$ such that

$$\begin{aligned} R_{\text{Earth}} + C_{\text{top}} - C_{\text{depth}} &\leq r \leq R_{\text{Earth}} + C_{\text{top}}, \\ 0 &\leq \phi \leq \frac{\psi}{2}, \\ 0 &\leq \theta \leq 2\pi, \end{aligned} \quad (5)$$

where R_{Earth} is the radius of the Earth. The geometry of cloud in the model is illustrated in Fig. 1, where the cloud is rotationally symmetric about the z -axis. Unless otherwise stated, in pencil beam simulations, the detector limb-view path is assumed to intersect the centre of the cloud top, to deal with the uncertainty in along limb cloud position.

The assumption of a spatially contiguous cloud is a necessary assumption as a disconnected cloud domain would add a further degree of complexity to the coupling of the clear sky and

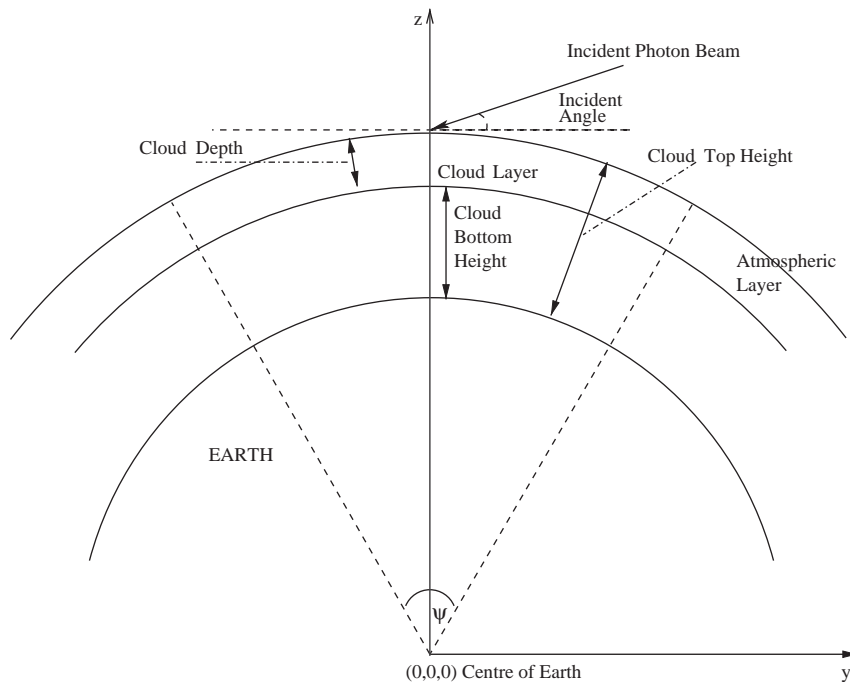


Fig. 1. 2-D Slice of cloud/Earth geometry.

scattering calculations, as well as having the implication that there could be an unquantifiable number of permutations of broken cloud field in the measurement inversion. This assumption is often valid, particularly for tropical and subvisible cirrus that has been observed in very thin unbroken layers which have a horizontal extent of the order of hundreds of kilometres [4,31–33]. The assumption of cloud as a uniform layer is often made in cloud retrieval schemes from remote measurements.

The finite extent of the cloud is chosen not to be included in the cloud state vector because limb-viewing instruments have a large uncertainty in cloud horizontal coverage along atmospheric paths [5]. Therefore, as the measurement inversion is unlikely to be able to retrieve the horizontal extent, it is instead included in the atmosphere state vector, $\hat{\mathbf{b}}$, and defined as the arc length of the cloud top derived from ψ and R_{Earth} .

In terms of Eq. (1) the cloud state vector is given by $\hat{\mathbf{x}}_{\mathbf{c}} = [r_{\mathbf{e}}, N, C_{\text{top}}, C_{\text{depth}}]$ for a given crystal habit.

2.1.3. Atmospheric model

A one-dimensional spherically symmetric atmosphere is assumed in the model, with an altitude grid resolution of 1 km. It is necessary to assume that the atmospheric properties are well known so that the line-by-line radiative transfer calculations of gaseous absorption and emission give accurate results. The temperature and pressure profiles can be taken from climatology data, the European Centre for Medium-Range Weather Forecasts (ECMWF) operational data or from retrieved profiles. Gas concentration profiles are taken from climatology, however a chemical transport model may give more representative information on trace gases. The source of atmospheric data used depends on the use of the model and the accuracy of the model output required.

In Eq. (1) the atmosphere state vector, $\hat{\mathbf{b}}$, contains the profiles of temperature, pressure and all relevant gases. In addition, the tangent height, t_h , of the limb viewing ray path (assumed to be well known) is also included in $\hat{\mathbf{b}}$ as is the temperature and emissivity of the Earth's surface, the radius of the Earth, the spectral range to be modelled, $[v_0, v_n]$ and the spectral resolution, $v_{\text{res}} = (v_n - v_0)/(n - 1)$ where n is the number of spectral points to model (i.e. the length of the synthesised measurement vector).

2.2. Reverse Monte Carlo scattering model

The Monte Carlo method has long been employed to solve the difficult problem of physically realistic light transport in a cloudy atmosphere [34–37].

Limb sounding only requires a very limited subset of outward propagation paths. Thus, the reverse Monte Carlo method is chosen because it allows all computational effort to be concentrated on calculating radiances for the desired line-of-sight. Furthermore, the reverse Monte Carlo model is chosen over alternative plane parallel methods, for example, discrete ordinates methods (e.g. DISORT [38]), as these are far more onerous to solve for the limb viewing geometry and have a computationally expensive requirement to calculate the whole radiation field. The reversed Monte Carlo method has been shown to be adept at dealing with the spherical atmosphere geometry necessary for limb sounding [39] and has been used recently for modelling

limb measurements of backscattered solar radiance (without specific account for clouds) [40] and for modelling microwave limb sounding measurements of cloud [41,42].

In McClouds_FM, the radiative transfer process in the cloud is considered as the stationary Markov chain whose states are photon interactions with cloud particles. Each interaction can have one of two outcomes: absorption or scattering of the photon, i.e. the photon path terminates or the photon leaves the interaction travelling in a new direction.

When simulating a pencil beam (in the backward direction from the detector), every photon in the beam enters the cloud at the same angle as given by the viewing geometry (which is defined by the tangent height, t_h , of the viewing ray path). Upon entry, each photon is traced through the cloud by determining the distance between interactions and the direction after scattering by generating random numbers¹ to sample the appropriate probability distributions until the photon is either absorbed or exits the cloud.

A generic Monte Carlo algorithm is used, as given in [44], with the appropriate probability distributions determined by the single scattering properties described in Section 2.1.1.

As the single scattering properties are dependent on the wavelength of infrared radiance the reverse scattering model holds for monochromatic radiation. If a high spectral resolution is required, then it is not practical for the scattering calculations to be done monochromatically at each spectral point. However, if the wavelength range to be simulated is relatively narrow (i.e. $< 0.25 \mu\text{m}$) then the scattering properties can be assumed constant across this range. Alternatively, if the range is wider, then the model is run at sampled points for which the single scattering properties have been calculated and then interpolating in the scattering output domain yields finer spectral resolution for McCloudS_FM calculations (see Section 2.4). At present, the single scattering properties are sampled at $0.25 \mu\text{m}$, as the complex refractive index of ice varies relatively smoothly at this resolution.

The reverse scattering model uses a large number ($\geq 10^6$) of photons in each pencil beam started at the detector, so that there is good statistical convergence and the model is still adequately fast. However, it is too demanding on computer memory and processing to store the exact path for each photon and calculate the radiance along it. Therefore, McClouds_FM makes a statistical estimate of the radiance from the photons scattered into the line-of-sight by focussing on a limited number of properties of the backward photon trajectories. First of interest is if the photon is non-divergent, i.e. neither scattered nor absorbed in the cloud domain. Secondly, if the photon is divergent, then it is determined if it exits the cloud base, the cloud top, or if it is absorbed in the cloud. Divergent photons escaping out of the cloud side are assumed lost as they are too complicated to account for in the model: the total number of photons is re-normalised to account for this. If the horizontal extent is large (see Section 3.2) and the vertical extent is relatively thin, it is found that very few photons exit the side of the cloud. An idea of the size of the error incurred from discarding the lost photons is given in Table 1. It can be seen that the induced error will be negligible for clouds with horizontal extent greater than 50 km. For photons which exit the cloud base or top, the exit angle with respect to the local horizontal (of the exit surface) is calculated. Only the polar angle is of interest as a spherically symmetric atmosphere is assumed and the

¹Currently, McClouds_FM uses the *ran2* random number generator given in [43]. The generator has a period length of approximately 2.3×10^{18} and is a combination of two Lehmer generators and a Bays-Durham shuffle to break up any serial correlations.

Table 1

Typical percentage of photons which exit the cloud side after scattering in a backward simulation

Horizontal extent of cloud (km)	Percentage of lost photons
10–20	1–3
20–50	0.2–1
50–80	0.05–0.2
80–110	0.01–0.05
> 110	<0.01

Figures are for a range of typical cirrus cloud optical properties ($\tau \simeq 0.1$) and viewing geometry, with a cloud depth of 1 km. The number of lost photons is weakly dependent on viewing geometry and decreases with physical cloud depth.

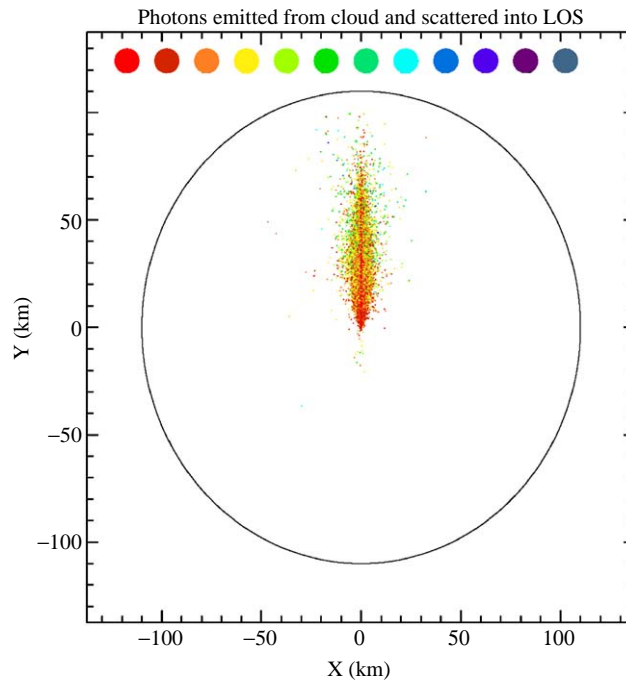


Fig. 2. FOV 'Footprint' on cloud top.

scattering is azimuthally isotropic. Finally, the terminal point of photons absorbed by the cloud are stored.

To reverse the simulated trajectories, the calculated photon exit angles out of the cloud top and bottom can be considered as the *entry* angles of photons entering the cloud and then being scattered into the line-of-sight, and the terminal location of photons absorbed inside the cloud can be considered the initial location of photons emitted from the cloud. Thus it can be seen that in the reverse of the simulation, there are four possible sources of radiation entering the (pencil-beam) line-of-sight from the cloud arriving at the detector: non-scattered from the direct limb path, scattered into the line-of-sight from below the cloud, scattered into the line-of-sight from above the cloud and emitted from within the cloud and scattered into the line-of-sight.

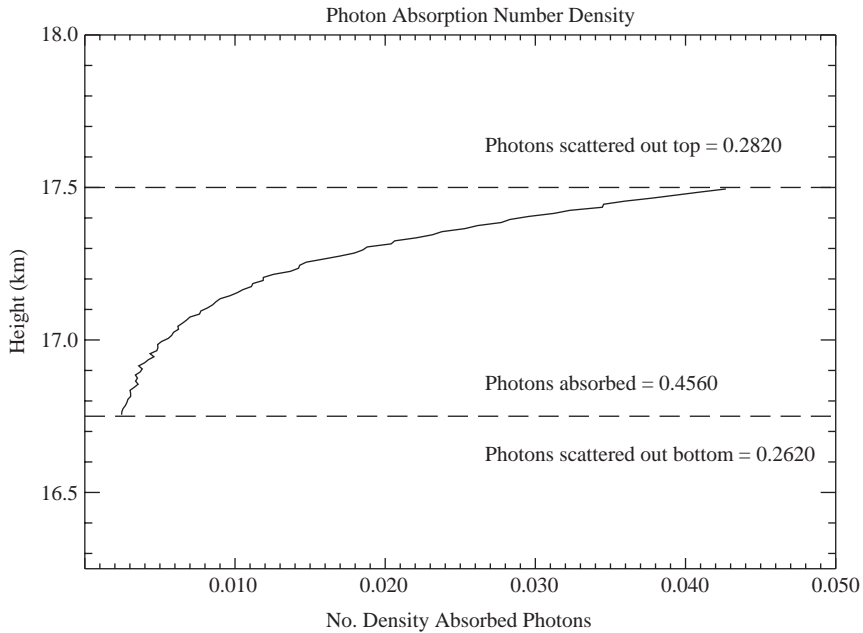


Fig. 3. The horizontal location of photons emitted from the cloud and scattered into the line-of-sight. The colour of each point indicates the number of scattering interactions each photon undergoes before entering the line of sight. Approximately 30% of emitted photons are scattered more than once. The satellite is located along the x -axis in the negative y direction.

Detailed information on the photon trajectories can be used to investigate the spread of photon source locations (see Fig. 2). As an example, scattering calculations were carried out for a cloud composed of hexagonal crystals with $\hat{\mathbf{x}}_c = [9.2 \mu\text{m}, 0.5 \text{cm}^{-3}, 17.5 \text{km}, 0.75 \text{km}]$ and for a viewing tangent height of 16.4 km and incident radiation of wavelength $10.75 \mu\text{m}$ ($\sim 930 \text{cm}^{-1}$). Fig. 2 shows the locations of photons emitted from the cloud and the degree of scattering each undergoes before leaving the cloud domain. For this particular cloud no photons escape from the cloud sides in the backward simulation, which can be seen from the emission points being located near the centre of the cloud. There is also a substantial degree of multiply scattered photons entering the limb path. Fig. 3 shows the equivalent vertical distribution of these photons and thus that the emission of photons from the cloud (that reach the limb) decays rapidly with height inside the cloud.

2.3. Radiative transfer in the clear sky domain

The radiative transfer calculations used in the clear sky domain in McClouds_FM are computed by the reference forward model (RFM). The RFM is a general line-by-line radiative transfer model based on GENLN2 [45] developed² by Dr. Anu Dudhia at the University of Oxford [47].

²Further details on the physical approximations used by the RFM can be found in [46].

The RFM performs the radiative transfer calculations (and ray tracing, inclusive of refraction if required) with user-specified measurement geometry, atmospheric model and spectroscopic data.

The radiance of photons arriving at the cloud bottom and cloud top is calculated by the RFM. This is done by the option in the RFM which allows the radiance arriving at an observer position in the atmosphere to be calculated for a given ‘elevation’ viewing angle i.e. the angle with the local horizontal at that altitude. This radiance calculated by the RFM is denoted, R_{obs} , and it can be described as a function of observer height (which will be C_{top} or C_{bot}), elevation angle, and wavenumber.

The RFM is also used to calculate the transmission and emission from the exit point from the cloud to the satellite, denoted $T_{\text{cld-sat}}(C_{\text{top}}, \phi_{\text{exit}}, \bar{\nu})$ and $R_{\text{cld-sat}}(C_{\text{top}}, \phi_{\text{exit}}, \bar{\nu})$ respectively. Where the exit angle, ϕ_{exit} , is the angle of incidence (measured with the respect to the local horizontal) of the viewing ray path with the cloud top.

As line-by-line calculations are being used to simulate measurement spectra, the convention is to define infrared radiation in terms of wavenumber, $\bar{\nu} = 1/\lambda$, as opposed to wavelength, λ .

2.4. McCloudS_FM calculations

For a given cloud in the model, i.e. with state parameter $\hat{\mathbf{x}}_{\text{c}} = [r_{\text{c}}, N, C_{\text{top}}, C_{\text{depth}}]$, the formulae used to combine the RFM calculations with statistical measures of the scattering output are given by:

- (1) Upwelling radiance from below the cloud redirected into the field-of-view:

$$R_{\text{bot}}(\bar{\nu}) = \sum_{i=1}^{N_{\phi}} \Phi_{\text{bot}}(i, \bar{\nu}) R_{\text{obs}} \left(C_{\text{bot}}, \phi_i - \frac{1}{2} \phi_{\text{bin}}, \bar{\nu} \right), \quad (6)$$

where $\Phi_{\text{bot}}(i, \bar{\nu})$ is the angular distribution of photons entering the cloud from its bottom and being scattered into the line-of-sight. $\Phi_{\text{bot}}(i, \bar{\nu})$ gives the fraction of photons entering from the bottom of the cloud which have entry angle ϕ in angle bin i i.e. $\phi \in [\phi_{i-1}, \phi_i)$. $N_{\phi} = 90^{\circ}/\phi_{\text{bin}}$ is the number of entry angle bins (ϕ_{bin} being the entry angle bin-size). $\Phi_{\text{bot}}(i, \bar{\nu})$ is determined from the Monte Carlo scattering calculations and can be thought of as the discrete pdf of bottom entry angle.

- (2) The downwelling radiance from above the cloud redirected into the field-of-view, R_{top} can be similarly defined

$$R_{\text{top}}(\bar{\nu}) = \sum_{i=1}^{N_{\phi}} \Phi_{\text{top}}(i, \bar{\nu}) R_{\text{obs}} \left(C_{\text{top}}, \phi_i - \frac{1}{2} \phi_{\text{bin}}, \bar{\nu} \right), \quad (7)$$

where $\Phi_{\text{top}}(i, \bar{\nu})$ is the discrete pdf of top entry angle.

- (3) Emission from within the cloud directed into the field-of-view;

$$R_{\text{cloud}}(\bar{\nu}) = \sum_{i=1}^{N_h} E_h(i, \bar{\nu}) B \left[T \left(h_i - \frac{1}{2} h_{\text{bin}} \right), \bar{\nu} \right], \quad (8)$$

where $E_h(i, \bar{\nu})$ is the emission density as a function of height. $E_h(i, \bar{\nu})$ gives the fraction of emitted photons which are emitted from a height h in height bin i i.e. $h \in [h_{i-1}, h_i)$. $N_h =$

$C_{\text{depth}}/h_{\text{bin}}$ is the number of emission height bins (h_{bin} being the entry angle bin-size). $E_h(i, \bar{\nu})$ and can be thought of as the discrete pdf of the source height of an emitted photon. $B[T, \bar{\nu}]$ is Planck's blackbody function which is calculated for the temperature $T = T(h_i - \frac{1}{2}h_{\text{bin}})$ at the mid-point of each height bin, derived from the temperature profile for the atmosphere. Planck's function is given by

$$B[T, \bar{\nu}] = \frac{c_1 \bar{\nu}^3}{\exp[c_2 \bar{\nu}/T] - 1} \quad (9)$$

in units of $\text{nW cm}^{-2} \text{sr}^{-1}(\text{cm}^{-1})^{-1}$, where $c_1 = 1.1911 \times 10^{-3} \text{ nW cm}^{-2} \text{sr}^{-1}(\text{cm}^{-1})^{-4}$ and $c_2 = 1.439 \text{ K}(\text{cm}^{-1})^{-1}$ for $\bar{\nu}$ in units of cm^{-1} and T in Kelvin, K .

(4) Radiance which will exit from the cloud in a pencil beam in the direction of satellite:

$$R_{\text{exit}}(\bar{\nu}) = f_{\text{bot}}(\bar{\nu})R_{\text{bot}}(\bar{\nu}) + f_{\text{top}}(\bar{\nu})R_{\text{top}}(\bar{\nu}) + f_{\text{cloud}}(\bar{\nu})R_{\text{cloud}}(\bar{\nu}), \quad (10)$$

where $f_{\text{top}}(\bar{\nu})$ ($f_{\text{bot}}(\bar{\nu})$) is the fraction of photons entering the cloud from its top (bottom) and scattered into the line-of-sight, and f_{cloud} is the fraction of photons emitted from the cloud entering the line-of-sight. Note that $f_{\text{top}}(\bar{\nu}) + f_{\text{bot}}(\bar{\nu}) + f_{\text{cloud}}(\bar{\nu}) = 1$.

(5) Finally the radiance at the satellite is calculated:

$$R_{\text{sat}}(\bar{\nu}) = (1 - f_0(\bar{\nu})) [R_{\text{exit}}(\bar{\nu})T_{\text{cld-sat}}(C_{\text{top}}, \phi_{\text{exit}}, \bar{\nu}) + R_{\text{cld-sat}}(C_{\text{top}}, \phi_{\text{exit}}, \bar{\nu})] + f_0(\bar{\nu})R_{\text{limb}}(t_h), \quad (11)$$

where $R_{\text{limb}}(t_h)$ is the radiance from emission along the limb viewing ray path with tangent height, t_h and calculated by the RFM, and $f_0(\bar{\nu})$ is the fraction of total photons in the pencil beam arriving at the satellite that are non-divergent or zeroth order, i.e. they are not scattered or absorbed in the cloud domain and pass directly through.

The main advantage of this method is that we retain the information on where the photons are coming from. We can see the proportion of the radiance arriving at the satellite that is from the cloud (emitting as a grey-body), and the proportion that has been scattered into the line-of-sight from above and below the cloud.

In terms of formulating McCloudS_FM as a function as in Eq. (1), the synthesised radiance measurement vector can be written as $\hat{\mathbf{y}} = \{\hat{y}(\bar{\nu}_0), \hat{y}(\bar{\nu}_1), \dots, \hat{y}(\bar{\nu}_n)\}$ where $[\bar{\nu}_0, \bar{\nu}_n]$ is the spectral range and $\bar{\nu}_i = \bar{\nu}_0 + i\bar{\nu}_{\text{res}}$ for $i = 0, 1, \dots, n$, where $\bar{\nu}_{\text{res}}$ is the spectral resolution. The synthesised measurement radiance, is given by

$$\hat{y}(\bar{\nu}_i) = R_{\text{sat}}(\bar{\nu}_i). \quad (12)$$

As stated in Section 2.2, if the spectral range required is relatively large then interpolation in the scattering output domain is required. If the single scattering properties for a given r_e and N have been calculated for a set of sampled wavenumbers i.e. $\{\bar{\nu}_{s_j} \in [\bar{\nu}_{s_0}, \bar{\nu}_{s_m}]: \bar{\nu}_{s_j} = \bar{\nu}_{s_0} + j\bar{\nu}_{s_{\text{res}}}; \frac{1}{\bar{\nu}_{s_{\text{res}}}} = 0.25 \mu\text{m}; j = 0, 1, \dots, m\}$ such that $[\bar{\nu}_0, \bar{\nu}_n] \subset [\bar{\nu}_{s_0}, \bar{\nu}_{s_m}]$, then the scattering calculations yield the discrete functions of two variables $\Phi_{\text{bot}}(i, \bar{\nu}_{s_j})$, $\Phi_{\text{top}}(i, \bar{\nu}_{s_j})$ and $E_h(i, \bar{\nu}_{s_j})$. These functions are then interpolated from the grid of $\bar{\nu}_{s_j}$'s at resolution $\bar{\nu}_{s_{\text{res}}}$ onto the grid of $\bar{\nu}_i$'s at resolution $\bar{\nu}_{\text{res}}$ to yield the discrete distributions $\Phi_{\text{bot}}(i, \bar{\nu}_j)$, $\Phi_{\text{top}}(i, \bar{\nu}_j)$ and $E_h(i, \bar{\nu}_j)$. These functions are then used in the empirical formulae (Eqs. (6)–(10) and (11)) outlined above to obtain the synthesised measurement vector.

2.4.1. Gaseous absorption and emission within the cloud domain

Due to computing limitations it is not practical to calculate the gaseous absorption and emission for each photon path inside the cloud domain. Thus, in order to include this in the model calculations several approximations must be made and this will result in additional forward model error.

McClouds_FM is currently configured to account for gaseous absorption and emission inside the cloud domain in one of three ways. The first being not at all and the McClouds_FM calculations are as set out previously. The second is to include only gaseous absorption and emission for photons entering the line-of-sight from below the cloud by making a crude approximation (for the purposes of the line-by-line calculations) of an infinitesimally thin cloud (often used in nadir sounding forward models), so Eq. (6) becomes

$$R_{\text{bot}}(\bar{\nu}) = \sum_{i=1}^{N_\phi} \Phi_{\text{bot}}(i, \bar{\nu}) R_{\text{obs}} \left(C_{\text{top}}, \phi_i - \frac{1}{2} \phi_{\text{bin}}, \bar{\nu} \right) \quad (13)$$

and the other equations remain unaltered.

The third method to account for gaseous absorption and emission inside the cloud domain uses the information from the scattering calculations on the total path length of each photon trajectory inside the cloud domain. From the atmospheric profiles of temperature, pressure and gas concentration, and using the RFM and the approximation that the temperature, pressure and gas concentrations are constant within the cloud domain it is possible to calculate the amount of absorption and emission for a path of a given length in the domain. However, it is still too computationally demanding to do this for every photon trajectory, so a statistical measure of path length is used. Photons scattered into the line-of-sight from below or above the cloud are binned by entry angle, and for each set of photons from a given entry angle bin the mean path length inside the cloud domain is calculated, denoted $L_{\phi_{\text{bot}}}(i, \bar{\nu})$ or $L_{\phi_{\text{top}}}(i, \bar{\nu})$. Likewise, photons emitted from the cloud and scattered into the line-of-sight are binned by emission height and for each height bin the mean path length inside the cloud domain of photons with that emission height is calculated as is the standard deviation, denoted $L_h(i, \bar{\nu})$. From the path length information the gaseous transmission and emission inside the cloud domain are calculated. This is then included in the McCloudS_FM calculations by changing Eq. (6) to

$$R_{\text{bot}}(\bar{\nu}) = \Phi_{\text{bot}}(i, \bar{\nu}) R_{\phi}^{L_{\text{bot}}}(i, \bar{\nu}) + \sum_{i=1}^{N_\phi} \Phi_{\text{bot}}(i, \bar{\nu}) T_{\phi}^{L_{\text{bot}}}(i, \bar{\nu}) R_{\text{obs}} \left(C_{\text{bot}}, \phi_i - \frac{1}{2} \phi_{\text{bin}}, \bar{\nu} \right), \quad (14)$$

where $R_{\phi}^{L_{\text{bot}}}(i, \bar{\nu})$ is the radiance of gaseous emission for the mean path length, $L_{\phi_{\text{bot}}}(i, \bar{\nu})$ of the photons which have entry angle ϕ in angle bin i i.e. $\phi \in [\phi_{i-1}, \phi_i)$ and $T_{\phi}^{L_{\text{bot}}}(i, \bar{\nu})$ is the gaseous transmission along the mean path length given by $L_{\phi_{\text{bot}}}(i, \bar{\nu})$. $R_{\text{top}}(\bar{\nu})$ can be similarly defined by changing *bot* to *top* functions in Eq. (14). Also, Eq. (8) must be changed to

$$R_{\text{cloud}}(\bar{\nu}) = E_h(i, \bar{\nu}) R_h^L(i, \bar{\nu}) + \sum_{i=1}^{N_h} T_h^L(i, \bar{\nu}) E_h(i, \bar{\nu}) B \left[T \left(h_i - \frac{1}{2} h_{\text{bin}} \right), \bar{\nu} \right], \quad (15)$$

where $R_h^L(i, \bar{\nu})$ is the radiance of gaseous emission for the mean path length, $L_h(i, \bar{\nu})$ of the photons which have emission height h in height bin i i.e. $h \in [h_{i-1}, h_i)$.

It is actually found that there is only a very small difference (usually $\sim 0.5\%$ in magnitude) between the radiance at the satellite calculated from the second and third methods of including gaseous emission and absorption in the cloud domain. As the second method requires far less computation time, the error margin is seen as acceptable to use method two to save on processing. However, it is more difficult to quantify the error incurred on line shape from the second method.

2.4.2. Forward model errors

It is important to quantify the accuracy of the forward model. However, when analysing the error budget it is important to distinguish between the error in quantifying the quality of the simulation given the assumptions about the cloud state, and the error incurred by the assumptions about the cloud state. Both of these error sources are then in turn independent from the error due to the sensitivity of the model to the atmosphere state parameters. This parameter error is not an error on the simulated radiance but can give an equivalent uncertainty on the modelled radiance for a specified uncertainty on an atmosphere state parameter.

This section will only consider the errors incurred by the forward model approximations to the physics of the radiative transfer for a cloud type as given in the model. The errors due to the assumptions (Section 2.1) about cloud type are essentially a problem for the measurement inversion and the accuracy of retrieved properties, which will not be considered here.

Table 2 lists the sources of errors in the model and the corresponding error in the simulated radiance. The difficulty in expressing the errors in this way is that the absolute value of the error is dependent on the both the input cloud state vector and the atmosphere state vector, as well as varying spectrally. The error values given in Table 2 are root-mean-square percentage errors in the at satellite radiance for $850\text{--}970\text{ cm}^{-1}$ and averaged over a range of cloud types (with a typical cirrus vertical optical depth of $\tau \simeq 0.1$), over a vertical profile of viewing geometries and using a tropical climatology for the atmospheric parameters.

Table 2 includes a simple photon counting error which is included to represent the Poisson statistics uncertainty in the number of photons per angle or height bin. The value given is for $\phi_{\text{bin}} = 1^\circ$ and $h_{\text{bin}} = 10\text{ m}$. Table 2 also includes the error in the simulated radiance due to the use of discrete angle and height bins, the error value is for $\phi_{\text{bin}} = 1^\circ$ and $h_{\text{bin}} = 10\text{ m}$, and is obtained by comparing against simulations with $\phi_{\text{bin}} = 0.001^\circ$ and $h_{\text{bin}} = 0.01\text{ m}$. The error incurred is negligible. Finally, Table 2 gives the error incurred from using the various methods to calculate the gaseous absorption for the photon paths inside the cloud domain (see Section 2.4.1). The error values given are for the various methods applied with $\phi_{\text{bin}} = 1^\circ$ and $h_{\text{bin}} = 10\text{ m}$ from comparison to calculations applied with $\phi_{\text{bin}} = 0.001^\circ$ and $h_{\text{bin}} = 0.01\text{ m}$ using method 3, so that there are very few photons per bin and thus the average path length per bin is more representative than for the larger bin size. The root-mean-square error for gaseous absorption is seen to be very small for each of the three methods, with the error mainly centred on the main gas lines, i.e. H_2O and CO_2 .

3. Considerations for simulating MIPAS measurements

Cirrus measurements made by limb observers are complicated by the non-continuous areal nature of clouds, and additional problems are manifested in the instrument field-of-view (FOV), the limb viewing and orbital geometry and the assumption of a one-dimensional (spherically

Table 2

Typical forward model errors for a range of typical cirrus cloud optical properties ($\tau \simeq 0.1$) and viewing geometry

Error source	Average percentage error
Poisson statistics	0.3
Discrete angle bins – $\phi_{\text{bin}} = 1^\circ$	0.1
Discrete height bins – $h_{\text{bin}} = 10$ m	0.05
Gaseous absorption in cloud (method 1)	0.7
Gaseous absorption in cloud (method 2)	0.35
Gaseous absorption in cloud (method 3)	0.2

symmetric) atmosphere in the measurement inversion. In this section, a brief introduction to the MIPAS instrument is given. This is followed by a discussion of the pertinent problems arising from the MIPAS measurements in order to develop the method to take the observing instrument into account in the forward model.

3.1. MIPAS

MIPAS was launched in March 2002, as part of the core payload of the European Space Agency Environmental Satellite (ENVISAT) polar-orbiter. MIPAS is a Fourier transform spectrometer designed for the monitoring of trace gas species by measuring high-resolution gaseous emission spectra at the Earth's limb. It operates in the near to mid infrared, ranging from 685 to 2410 cm^{-1} (4.15–14.6 μm).

MIPAS can collect data from various altitudes and various positions by using two scanning mirrors to point at different angles to the side and to the rear of ENVISAT. The nominal scan mode is in the anti-flight direction. In nominal mode the vertical range is approximately 6–68 km, with 17 elevation scans making up an elevation profile. Vertical spacing between scans is 3 km for 6–42 km, increasing to 6 km spacing between 42–60 km and finally 8 km between the penultimate and highest scan. At the tangent point, the Instantaneous FOV of MIPAS is about 3 km in elevation by 30 km in azimuth.

3.2. Effective horizontal cloud extent

Limb sounders may be able to detect cloud somewhere along the very long atmospheric path length, but they cannot determine how much of the path length is occupied by the cloud.

If a spherical atmosphere is assumed, composed for example of spherical atmospheric shells, say 1 km thick, then the layer containing the tangent point of the limb path contributes the most information to the measurement and (around the mid-troposphere) has a volume sample length of approximately 200 km. In limb occultation detection the measurement is of cloud extinction along the ray path, so a common method of dealing with uncertainty in horizontal coverage is to assume that the cloud field is restricted to the length of the tangent layer volume sample length, or to assume an effective horizontal extent, for example 75 km [6]. For infrared limb emission to incorporate limb scattering a similar approximation of horizontal coverage can be made to account for the effective scattering volume.

It can be seen from [Table 1](#) that all clouds with horizontal extent greater than 110 km ‘look’ the same to a pencil beam incident on the centre of the cloud top, in that a negligible number of photons is scattered out of the sides of the cloud, hence the scattering output is not influenced by the horizontal extent. Therefore, by setting the horizontal extent as 200 km, in line with the volume sample length in the tangent layer, it has the effect of modelling the scattering from a pencil beam for all cloud with horizontal extent greater than 110 km. Effectively this models optically thin cloud without distinct (sharp) side boundaries (horizontal edges), which is physically more realistic. This model limit on cloud extent has several implications if applied to the physics of the limb measurement.

3.3. The instrument field-of-view

Problems begin to be encountered when the FOV ‘Footprint’ is not filled. This can occur in three ways: if the cloud horizontal extent is less than the FOV Footprint, or if the cloud is of large horizontal extent but the viewing tangent height is too high or too low for the FOV ‘Footprint’ to be entirely cloud filled. When the cloud is of large horizontal extent but the viewing geometry is incorrect for the FOV ‘Footprint’ to be entirely cloud filled, the FOV effect can be accounted for by using clear sky radiative transfer for the pencil beams in the FOV which do not emerge from the cloud. There is a large uncertainty when modelling cases in which the cloud extent is less than the FOV ‘Footprint’ or the viewing tangent height is too low due to lost photons. As a result of these errors, a measurement inversion is likely to be insensitive to cloud position within the FOV (or more specifically to have multiple solutions with high error). Therefore, when simulating MIPAS data, the case where the FOV ‘Footprint’ is not entirely filled is only modelled when the viewing tangent height is too high. Furthermore, the effective horizontal extent of the cloud is assumed to be greater than the Footprint and of the order of 200 km, in line with the limit of accuracy mentioned in Section 3.2. Therefore, this work is focussed on modelling limb observations of cirrus of large horizontal extent. And any comparisons to MIPAS data are in the assumption that the observed cirrus is of large horizontal extent.

This assumption should not be considered a drawback, as cirrus is usually much greater in horizontal extent than vertical extent. For example, the Lidar In Space Technology Experiment (LITE) [33] detected laminar cirrus with a horizontal extent of <100 km up to 2700 km and thickness of less than 200 m in an altitude region of 14–18.7 km. Orographic and convective cirrus have frequently been observed with horizontal extent on the order of hundreds of kilometres, e.g. [48] and jet stream cirrus can cross continents nearly unbroken with a vertical depth of only a few kilometres.

The assumption that any *observable* cirrus is of a large horizontal extent also resolves the uncertainty of the cloud limb position. If the cloud top height is higher than tangent height then it can be assumed that the limb observation is ‘seeing’ the cloud top, i.e. the ray path intersects with the cloud top.

4. Model comparisons to data

In order to validate the McClouds_FM simulated satellite measurements the model output was compared to real MIPAS measurements of cirrus. The atmospheric window region was of main interest as the transparency of the atmosphere allows the photons from the scattered ray paths to originate from lower in the atmosphere, i.e. from warmer temperatures, and thus the evidence of scattering should be more apparent. In this study attention was particularly focussed on modelling the absorbing H₂O lines due to scattering, in the region 940–950 cm⁻¹ (following [16,17]).

4.1. MIPAS data

The MIPAS data used in this case study is from orbit 504 from the 16th of May 2002. MIPAS spectra is measured in five spectral bands (see Table 3) at a spectral resolution of 0.025 cm⁻¹, which non-continuously span the spectral range 685–2410 cm⁻¹. Only band A (685–970 cm⁻¹) data was used in this case study as this covers the main atmospheric window region of interest.

Table 3
The spectral ranges of the MIPAS bands

Band	Wavenumber range (cm ⁻¹)
A	685–970
AB	1020–1170
B	1215–1500
C	1570–1750
D	1820–2410

For cirrus cloud observations, attention was focused on elevation profiles from tropical regions where it is well known that high cirrus frequently occurs, as does subvisible cirrus near the tropopause.

It is reasonably easy to determine the presence of cloud qualitatively in MIPAS scans at tangent heights in the region 12–18 km, as those which have evidence of a strongly increased broadband continuum signal in the atmospheric window region of the spectra. However, for fringe cases such as subvisible cirrus it becomes a little more difficult, so a simple thresholding method was applied. The radiances for each elevation scan at 960.7 cm⁻¹ were compared to a threshold in order to determine whether or not cloud was present in that particular scan. This wavenumber was chosen as it is in a window region and should therefore have a very low radiance, unless some emitting (or scattering) body is present. The threshold could be based on calculated expected radiance for varying atmospheric properties and temperature profiles, however due to the low radiances expected from this wavenumber an absolute threshold (at a low level) can be used to good effect, in this case 105 nW cm⁻² sr⁻¹(cm⁻¹)⁻¹. This value was determined from statistical studies of MIPAS data. The expected detection sensitivity of MIPAS to cloud optical depth at this threshold has been investigated through simulated studies and is discussed in Section 4.4.

The elevation profile selected for use in this case study has a mean tangent point location at a Latitude of 1.25°N and a Longitude of 36.5°E. The measurement spectra of two elevation scans from tangent heights of 13.54 and 16.42 km can be seen in Figs. 5 and 6, respectively. The inverted spectral lines due to scattering of tropospheric radiation into the FOV can be clearly seen at ~948.25 cm⁻¹.

The scattering features under investigation i.e. the H₂O absorption lines and the inverted CO₂ side-lobes, are spectrally very narrow and as MIPAS is a Fourier transform spectrometer it is important to be sure that any such features in the measured spectra cannot be due to instrument line shape (ILS) artefacts. Therefore, only the *apodised* MIPAS spectra are used for the comparisons to the model output. The MIPAS apodised spectra are produced using an ILS with the Norton-Beer ‘strong’ apodisation applied [49].

4.2. Initial comparisons to data

The measurement spectra from the elevation scans at 13.56 and 16.42 km are denoted by the vectors \mathbf{y}_{13} and \mathbf{y}_{16} and are composed of $N_{\bar{\nu}} = ((950 - 940)/0.025) + 1$ spectral points. For each measurement vector in turn, a cloud state ($\hat{\mathbf{x}}_c = [r_c, N, C_{\text{top}}, C_{\text{depth}}]$) was estimated (assuming

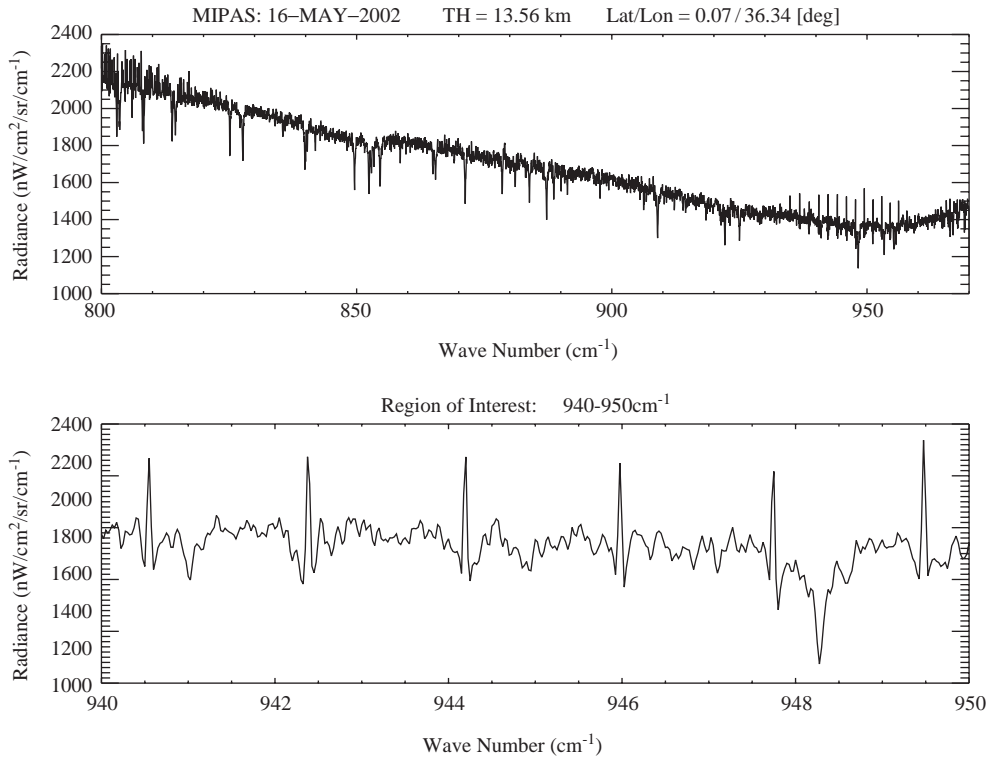


Fig. 5. McClouds_FM simulated spectra for \hat{x}_{13} using ECMWF temperatures. The (blue) dot-dash line is $f_{bot} R_{bot}$, the radiance scattered into the line-of-sight from photons from below the cloud. The (green) dotted line is $f_{top} R_{top}$, the radiance scattered into the line-of-sight from photons from above the cloud. The (red) dashed line is $f_{cloud} R_{cloud}$, the radiance of photons emitted from the cloud and scattered into the line-of-sight. The (black) solid line is $R_{exit} = f_{bot} R_{bot} + f_{top} R_{top} + f_{cloud} R_{cloud}$.

hexagonal column crystal habit) and McClouds_FM was used to simulate the spectra (with a 3-beam FOV) obtaining \hat{y}_{13} and \hat{y}_{16} , respectively. After each simulated spectra was generated, the goodness-of-fit to the measurement was tested and if the fit did not meet a certain criteria the cloud state was altered systematically and the spectra simulated again. This process was iterated (over a finite set of cloud property permutations) until a “best-fit” spectra was obtained.

The goodness-of-fit was measured by the quantity

$$\chi^2 = \sum_{i=1}^{N_{\bar{v}}} \frac{|y(\bar{v}_i) - \hat{y}(\bar{v}_i)|^2}{\varepsilon_y(\bar{v}_i)^2}, \quad (17)$$

where $y(\bar{v}_i)$ is the MIPAS measured radiance at the spectral point \bar{v}_i , $\hat{y}(\bar{v}_i)$ is the modelled radiance value from McClouds_FM at the spectral point \bar{v}_i , and $\varepsilon_y(\bar{v}_i)^2$ is the uncertainty in $y(\bar{v}_i)$ from the measurement error, i.e. the noise equivalent signal radiance which in Band A is $50 \text{ nW cm}^{-2} \text{ sr}^{-1} (\text{cm}^{-1})^{-1}$. As a general rule, for a given number of degrees of freedom, df , one wants the “reduced χ^2 ” (χ^2/df) to be approximately equal to one ($\chi^2 \sim df$). A reduced χ^2 that is

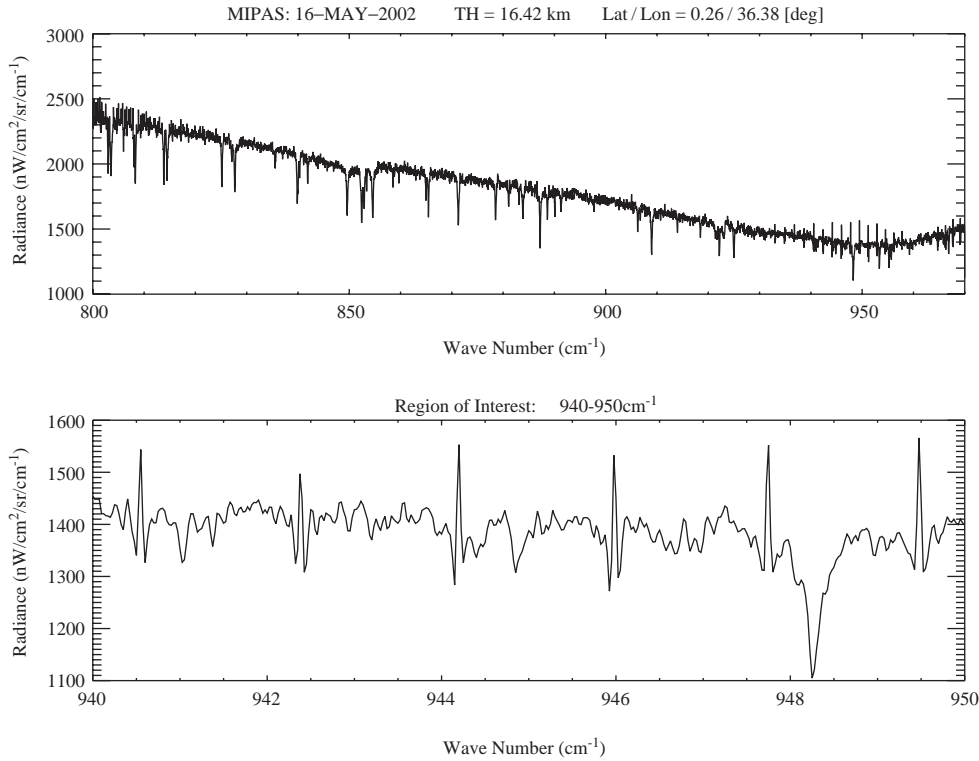


Fig. 6. McCloudS_FM simulated spectra for \hat{x}_{16} using ECMWF temperatures. The linestyle and colour key is the same as in Fig. 5.

much greater than one indicates a poor fit. In this case, if we assume that for the vectors \mathbf{y} and $\hat{\mathbf{y}}$, each spectral point in the vector is independent from all other points in the vector, then the number of degrees of freedom is $df = N_{\hat{\mathbf{y}}} - 1$. The “best-fit” spectra is such that it minimises the χ^2 value.

In order to compare the McClouds_FM output against the apodised MIPAS data, the simulated spectra must also be apodised by post-processing. This post-processing involves convolving the spectra simulated by McClouds_FM at high resolution ($\bar{\nu}_{\text{res}} = 0.001 \text{ cm}^{-1}$) for each of the elevation scans, with an ILS function³ for MIPAS band A measurements, then down-sampled to the resolution of the measurement spectra.

The “best-fit” search process was carried out with the gas concentration profiles taken from reference atmosphere climatology [50], and the temperature and pressure profiles obtained from ECMWF data. The viewing tangent heights of 13.56 and 16.42 km are taken from the nominal MIPAS level 1B tangent heights derived from the MIPAS pointing information. They are assumed to be accurate here (see Section 4.3 for further comment).

³Obtained via private communication from Dr. Chiara Piccolo, University of Oxford.

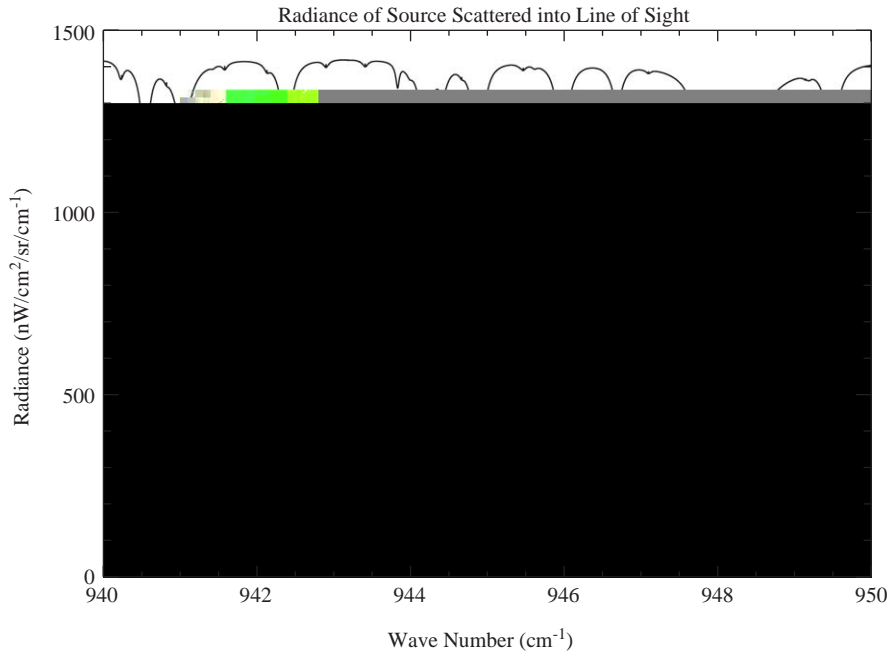


Fig. 7. McCloudS_FM simulated apodised spectra for $\hat{\mathbf{x}}_{13}$ using ECMWF temperatures: the dot-dashed (red) line is the multiple scattering case and single scattering case is the dashed (green) line. The measurement spectra $\hat{\mathbf{Y}}_{13}$ is the solid (black) line .

It was found that the best-fit spectra, were obtained from cloud state vectors of

$$\hat{\mathbf{x}}_{13} = [11.75 \mu\text{m}, 2.75 \text{ cm}^{-3}, 18.75 \text{ km}, 0.5 \text{ km}]$$

and

$$\hat{\mathbf{x}}_{16} = [7.85 \mu\text{m}, 4.76 \text{ cm}^{-3}, 18.75 \text{ km}, 0.7 \text{ km}],$$

respectively.

Figs. 7 and 8 show the breakdown (for the central beam of the FOV in the $\hat{\mathbf{x}}_{13}$ and $\hat{\mathbf{x}}_{16}$ simulations respectively) of the radiance from the various sources which is scattered into the line-of-sight i.e. the quantities, $f_{\text{bot}}R_{\text{bot}}$, $f_{\text{top}}R_{\text{top}}$, $f_{\text{cloud}}R_{\text{cloud}}$ and R_{exit} as given in Eqs. (6)–(8), and (10).

The simulated radiance arriving at the satellite, $\hat{\mathbf{y}}_{13}$ and $\hat{\mathbf{y}}_{16}$ is graphed in Figs. 9 and 10, respectively, with the MIPAS measurement overplot as well as the radiance obtained from the same simulation but with only single scattering. Both Figs. 9 and 10 illustrate clearly that without multiple scattering included in the simulation the radiance can be grossly underestimated by around 15–20%. In addition, it is possible to see that the H_2O absorption features are recreated in the simulation and from Figs. 7 and 8 it can be seen that the only source of these absorption features is from radiance scattered into the line-of-sight from below the cloud, which accounts for approximately 40% of the radiance exiting the cloud.

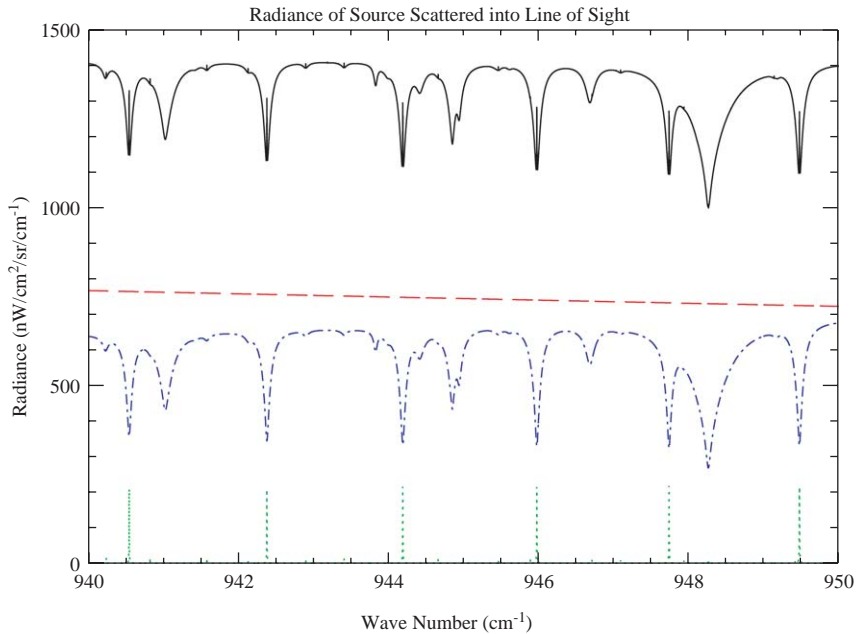


Fig. 8. McCloudS_FM simulated apodised spectra for \hat{x}_{16} using ECMWF temperatures: the dot-dashed (red) line is the multiple scattering case and single scattering case is the dashed (green) line. The measurement spectra \hat{Y}_{13} is the solid (black) line.

Finally, Figs. 11 and 12 give the percentage difference between the apodised radiance at the satellite and the apodised MIPAS measurement spectra. The root-mean-square (rms) percentage difference and rms noise percentage are both overplot on the figures. It can be clearly seen that the rms percentage difference is less than the rms measurement noise percentage. Therefore, it is possible to obtain convergence for the cloud state values from which McClouds_FM can successfully model MIPAS spectra within measurement noise. Furthermore, the percentage residual in Figs. 11 and 12 is less than the noise level in $\sim 85\%$ of the simulated spectral window. The outlying points being centred around the H_2O absorption features, but do not exceed a difference of 13% from the measurement in either case.

4.3. Discussion

Interestingly, the cloud top was found to be slightly higher than the tropopause by approximately 0.5 km. Also, the cloud vector for the \hat{y}_{13} simulation has a smaller effective radius and larger number density than the cloud vector for the \hat{y}_{16} best-fit simulation. It is not unreasonable to expect that this is a physical difference. Due to the integration time of each tangent height measurement the horizontal distance between tangent points can be up to 30 km, therefore it is possible that the cloud is horizontally inhomogeneous on such a scale.

The “best-fit” spectra discussed above are only best-fit in the sense that they have the lowest χ^2 value for a set of spectra generated from a finite set of cloud property permutations. Moreover, it is not to say that there are no other permutations which could generate a simulated spectra which

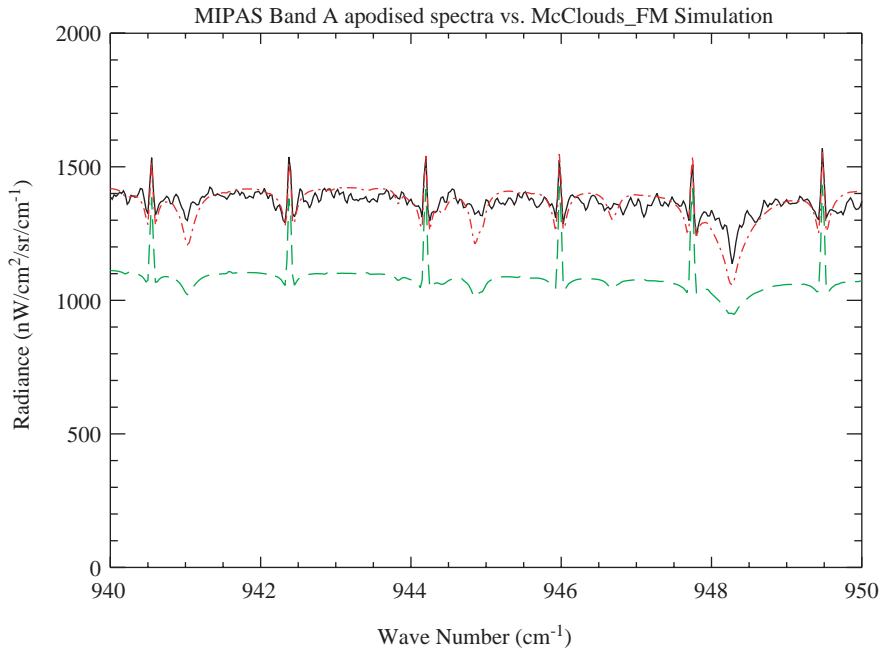


Fig. 9. McCloudS_FM simulated spectra for $\hat{\mathbf{x}}_{13}$ using ECMWF temperatures. The percentage difference between the simulated apodised radiance and the 13.54 km MIPAS measurement. The straight dashed (red) line is the root mean square uncertainty due to measurement noise and the lower dot-dashed (blue) line is the root mean square percentage difference.

would have a smaller χ^2 and model the spectra more accurately than in the cases above. This is important to realise as it points the way to adopting an optimal estimation or “retrieval” technique in order to use the inherent information in the forward model in a more efficient manner to iterate to the point in the infinite 4D cloud state space which would give the best-fit simulated spectra. This argument could also be extended to explain the difference between the $\hat{\mathbf{x}}_{13}$ and $\hat{\mathbf{x}}_{16}$ cloud vectors.

The radiance in the McClouds_FM simulations is too low around the H₂O absorption features compared to the MIPAS measurements. Thus, the absorption features are slightly too broad, which suggests that McClouds_FM may be overestimating the radiance scattered in from below the cloud, which is the source of the absorption lines. However, a more likely source of this error could be due to the use of climatology data for the gas concentration profiles. If the H₂O amounts are slightly inaccurate in the atmospheric model it will lead to discrepancies between model output and the data at the major lines.

The simulations were carried out without gaseous absorption (and emission) within the cloud domain. This was again done for simplicity to reduce the number of calculations required. However, the lack of gaseous absorption could explain both the missing fine structure in the simulations and the slightly larger discrepancy around the absorption features. The small numbers in Table 2 for error due to gaseous absorption inside cloud, corroborate this explanation, as they are rms errors and (as mentioned in Section 2.4.2) the main error is centred about the main gas spectral lines, i.e. H₂O and CO₂.

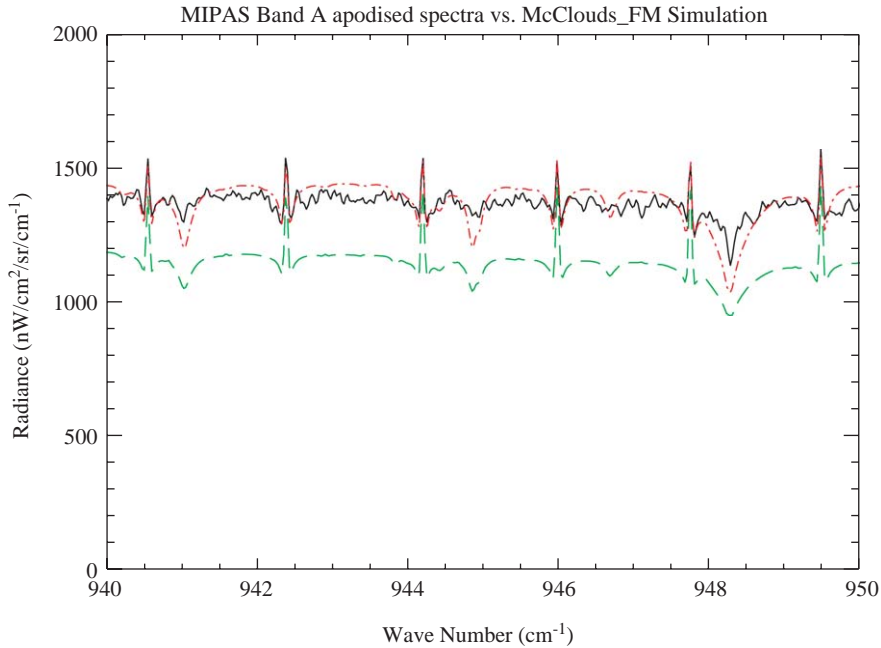


Fig. 10. McCloudS_FM simulated spectra for \hat{x}_{16} using ECMWF temperatures. The percentage difference between the simulated apodised radiance and the 16.42 km MIPAS measurement. The straight dashed (red) line is the root mean square uncertainty due to measurement noise and the lower dot-dashed (blue) line is the root mean square percentage difference.

Another reason that the simulation may not match the measurement as well at the absorption features is that the viewing tangent height returned by the MIPAS pointing information is only certain to within $\sim \pm 1.5$ km. Changing the tangent height in the simulations will change the scattering geometry (though only to a small degree as the radius or curvature in the spherical geometry is large). This in turn can alter the magnitude of the effect of warm photons scattering into the line-of-sight from below the cloud and hence the size of the absorption features. An example of this effect is given in Fig. 15. It can be seen that by differing the tangent height by 1 km the simulated radiance at the satellite can differ by up to $\sim 7.5\%$, but interestingly the differences are smallest at the absorption features. This could prove a large error source in the quality of fit of the McClouds_FM simulation to the MIPAS data. However, this is a parameter error and is essentially a problem for the measurement inversion, as the cloud state vector can be changed to give a better simulation for the correct tangent height. In addition, the uncertainty in tangent height can be improved by using the pressure from the MIPAS operational retrievals which is accurate to 1%, then using the ECMWF geopotential pressures to obtain a more accurate tangent height value.

4.4. Detection sensitivity

Now that it has been shown that McClouds_FM can model cirrus contaminated MIPAS measurements well, using realistic cloud fields, McClouds_FM can be used to investigate the

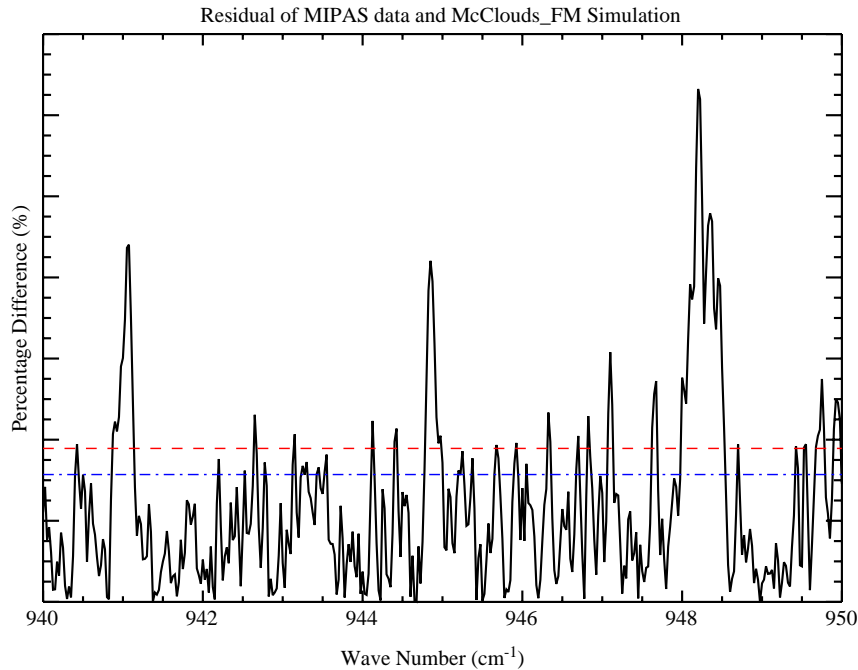


Fig. 11. McCloudS_FM simulated spectra for \hat{x}_{13} using ECMWF temperatures. The percentage difference between the simulated apodised radiance and the 13.54 km MIPAS measurement. The straight dashed (red) line is the root mean square uncertainty due to measurement noise and the lower dot-dashed (blue) line is the root mean square percentage difference.

potential cloud detection sensitivity of MIPAS. By simulating the radiance across the detection threshold at $\bar{\nu} = 960.7 \text{ cm}^{-1}$ for a wide of range of optical depths of cloud, the minimum optical depth that can be detected can be investigated. Fig. 13 shows the radiance at the threshold for cloud effective radius versus vertical optical depth, for a simulation with the cloud top height at 18.0 km and the viewing tangent height at 16.42 km. The figure clearly shows that cloud is detectable (above measurement noise) for optical depths of 0.002. This high sensitivity to optical depth is due to the multiple scattering enhancement. In addition, an interesting result is that the multiple scattering effect actually peaks at an optical depth of about 0.1 (increasing slightly at higher effective radii), then decreases and levels off at higher optical depths. This is because at low optical depths (< 1.0) warm photons from lower in the atmosphere are scattered into the line-of-sight, and as the optical depth increases up to 0.1, the number of ice crystals increases and hence the strength of multiple scattering increases causing a radiance increase until a peak effect of scattering is reached. As the cloud becomes optically thicker the radiance decreases as the satellite detector sees less of the warm photons which are now being absorbed within the cloud. Eventually, as the optical depth increases further the satellite is only seeing the colder photons from the cloud top and the radiance levels off and in effect the satellite is only sensitive to the cloud top temperature.

The enhancement of multiple scattering over single scattering for the same cloud scenarios that produced Fig. 13, can be seen in Fig. 14. It can be seen that the peak multiple scattering effects

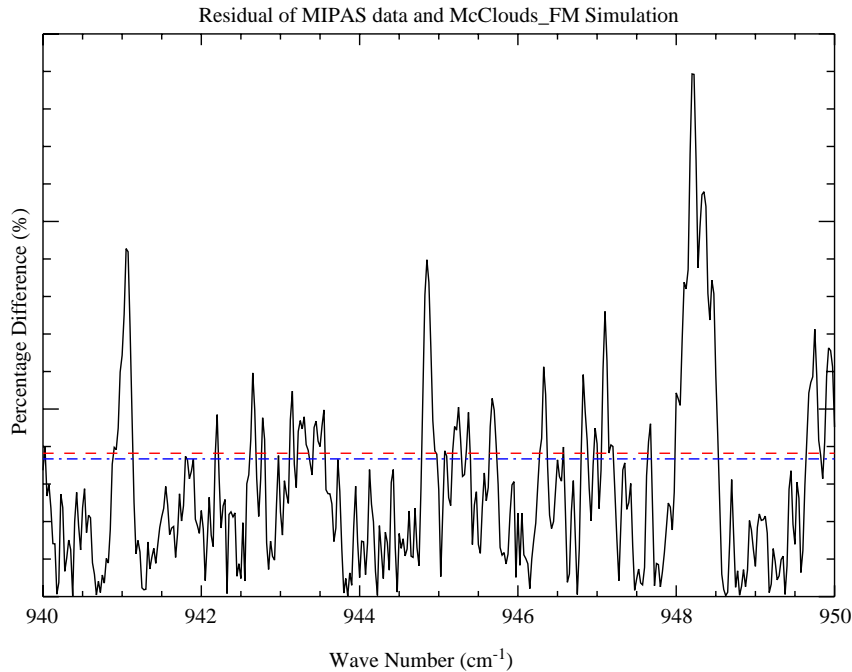


Fig. 12. McCloudS_FM simulated spectra for \hat{x}_{16} using ECMWF temperatures. The percentage difference between the simulated apodised radiance and the 16.42 km MIPAS measurement. The straight dashed (red) line is the root mean square uncertainty due to measurement noise and the lower dot-dashed (blue) line is the root mean square percentage difference.

occur at optical depths of around 0.1 and can cause radiances of up to 25% greater than single scattering alone. This is a powerful result and clearly illustrates the importance of including multiple scattering in the radiative transfer.

5. Conclusions

The results from McClouds_FM have shown that for realistic cloud fields can be iterated to such that the MIPAS spectra with cirrus in the FOV can be well modelled to within instrument noise. Additionally, the root mean square difference of the modelled spectra and the limb measurements is below 5%, thus meeting the initial aim for spectral accuracy requirements. Therefore, under the assumptions made in the model it can be expected that the cloud state parameters are a good first order approximation to the real cirrus. Further, the H₂O absorption lines are replicated in the McClouds_FM simulated spectra and (from Figs. 7 and 8) it can be seen that these absorption features are clearly due to tropospheric radiation from below the cloud, and below the limb path being scattered into the instrument line-of-sight.

The results have also shown that simulated spectra under single scattering into the line-of-sight significantly underestimates the radiance arriving at the satellite. This clearly states the case for the inclusion of multiple scattering within cloudy regions in the limb radiative transfer calculations.

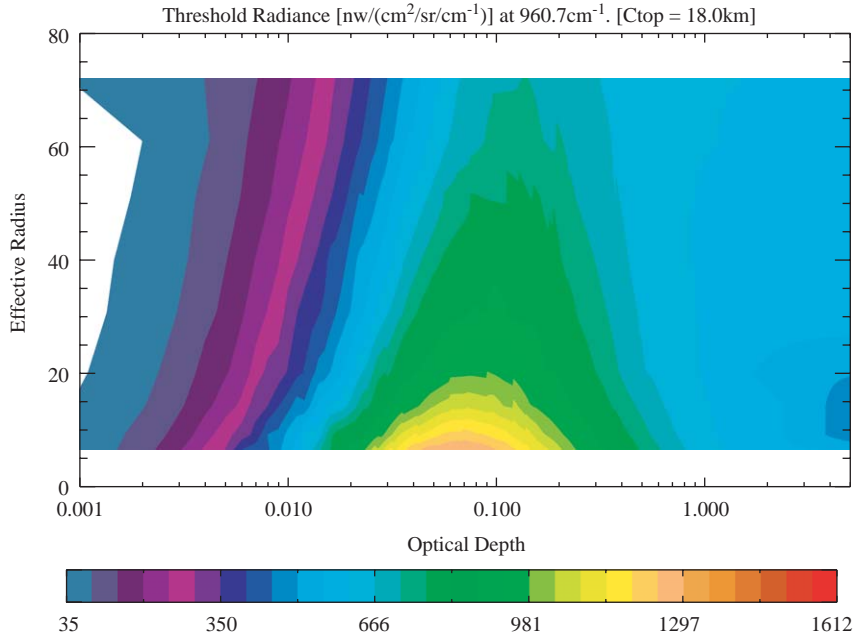


Fig. 13. Percentage residual between a pencil beam simulation for \hat{x}_{16} at a tangent height of 16.42 km and simulations with a tangent height of 15.42 km (dot-dash line in red) and 17.42 km (solid line in black).

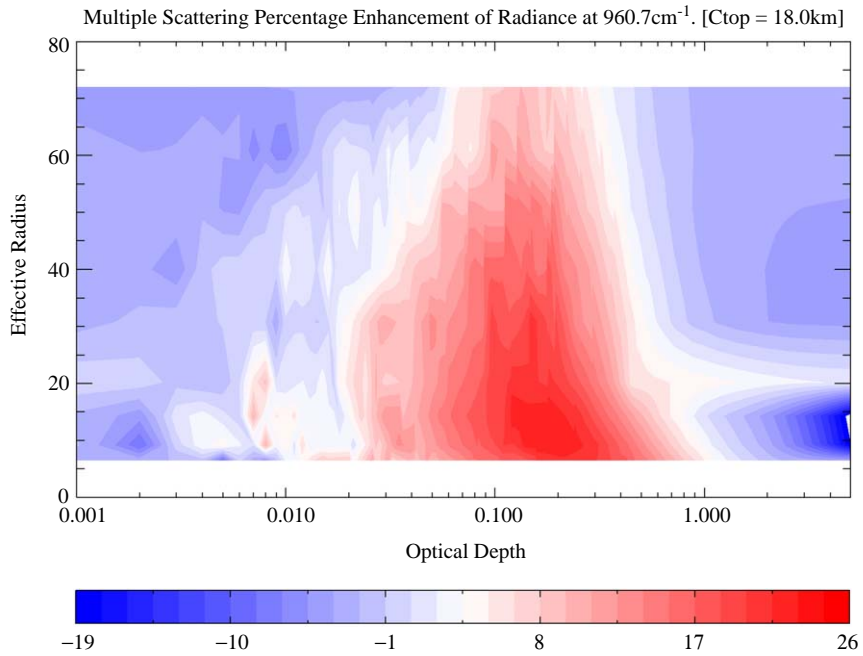


Fig. 14. Percentage enhancement of multiple scattering over single scattering McClouds_FM calculated radiance at 960.7 cm^{-1} for various cloud types with cloud top at 18.0 km and a viewing tangent height of 16.42 km.

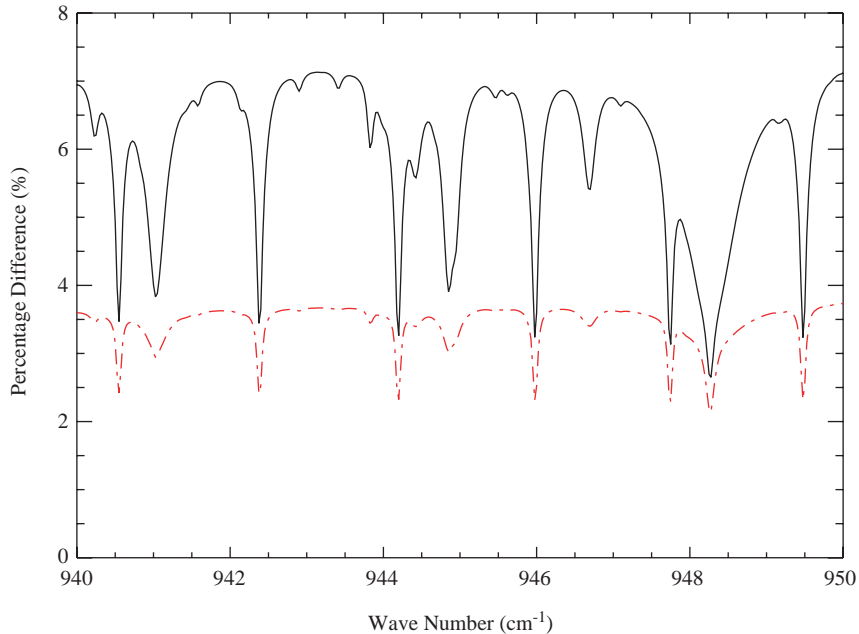


Fig. 15. Percentage residual between a pencil beam simulation for \hat{x}_{16} at a tangent height of 16.42 km and simulations with a tangent height of 15.42 km (in red) and 17.42 km (in black).

6. Future work

Plans are already in place to use `McClouds_FM` operationally in a retrieval scheme to derive macrophysical and microphysical properties of cirrus from MIPAS measurements. By using the model within such an algorithm, the retrieved cloud properties could be compared against co-located external cloud property data sets, e.g. those derived from AATSR (the Advanced Along Track Scanning Radiometer) which also flies on *EnviSat*, in order to validate the model and retrieval results. It will also be important, within such a scheme, to investigate the differences in retrieved results depending on the ice crystal habit assumed.

For future studies, `McClouds_FM` should be implemented to use the MT19937 Mersenne Twister pseudo-random number generator [51], in place of the one used currently. This will give a 623-dimensional equidistribution with a period length of $2^{19937} - 1$.

Acknowledgements

The authors would like to acknowledge both the Natural Environment Research Council and the Global Retrieval of ATSR-2 cloud Products and Evaluation (GRAPE) Project for the funding of this work.

References

- [1] Wylie DP, Menzel WP, Woolf HM, Strabala KL. Four years of global cirrus cloud statistics using HIRS. *J Climate* 1994;9:1972–86.
- [2] Liou KN. Influence of cirrus clouds on weather and climate processes: a global perspective. *Mon Weather Rev* 1996;114:4289–98.
- [3] Stephens GL, Tsay S-C, Stackhouse Jr PW, Flatau PJ. The relevance of the microphysical and radiative properties of cirrus clouds to climate and climate feedback. *J Atmos Sci* 1990;47:1742–53.
- [4] Dowling DR, Radke LF. A summary of the physical properties of cirrus clouds. *J Appl Meteor* 1990;29:970–8.
- [5] Liao X, Rossow WB, Rind D. Comparison between SAGE II and ISCCP high-level clouds 1. Global and zonal mean cloud amounts. *J Geophys Res* 1995;100(1):1121–35.
- [6] Liao X, Rossow WB, Rind D. Comparison between SAGE II and ISCCP high-level clouds 2. Locating cloud tops. *J Geophys Res* 1995;100(2):1137–47.
- [7] Massie S, Randel W, Wu F. Halogen occultation experiment and stratospheric aerosol and gas experiment II observations of tropopause cirrus and aerosol during the 1990s. *J Geophys Res* 2003;108:4222–33.
- [8] Wang P-H, Minnis P, McCormick MP, Kent GS, Skeens KM. A 6-year climatology of cloud occurrence frequency from stratospheric aerosol and gas experiment II observations (1985–1990). *J Geophys Res* 1996;101:407–29.
- [9] McFarquhar GM, Heymsfield AJ, Spinhime J, Hart B. Thin and subvisual tropical and tropopause cirrus: observations and radiative impacts. *J Atmos Sci* 2000;57:1841–53.
- [10] Jensen EJ, Pfister L, Ackerman AS, Tabazadeh A, Toon OB. A conceptual model of the dehydration of air due to freeze-drying of optically thin laminar cirrus rising slowly across the tropical tropopause. *J Geophys Res* 2001;106:17237–52.
- [11] Woodbury GE, McCormick MP. Global distributions of cirrus clouds determined from SAGE data. *Geophys Res Lett* 1983;10:1180–3.
- [12] Hervig M, McHugh M. Cirrus detection using HALOE measurements. *Geophys Res Lett* 1999;26:719–22.
- [13] Kahn BH, Eldering A, Irion W, Mills FP, Sen B, Gunson MR. Cloud identification in atmospheric trace molecule spectroscopy infrared occultation measurements. *Appl Opt* 2002;41:2768–80.
- [14] Mergenthaler JL, Roche AE, Kumer JB, Ely GA. Cryogenic limb array etalon spectrometer observations of tropical cirrus. *J Geophys Res* 1999;104:183–94.
- [15] Spang R, Eidmann G, Riese M, Offerman D, Preusse P. CRISTA observations of cirrus clouds around the tropopause. *J Geophys Res* 2002;92(D23):8174.
- [16] Hopfner M, Oelhaf H, Wetzel G, Friedl-Vallon F, Kleinert A, Lengel A, Maucher G, Nordmeyer H, Glatthor N, Stiller G, von Clarmann T, Fischer H, Kroger C, Deshler T. Evidence of scattering of tropospheric radiation by PSCs in mid-IR limb emission spectra: MIPAS-B observations and KOPRA simulations. *Geophys Res Lett* 2002;29(8).
- [17] Spang R, Remedios JJ, Barkley MP. Colour indices for the detection and differentiation of cloud types in infra-red limb emission spectra. *Adv Space Res* 2004;33:1041–7.
- [18] Höpfner M. Study of polar stratospheric clouds on high resolution mid-IR limb emission spectra. *JQSRT* 2004;83:93–107.
- [19] Heymsfield AJ, Miloshevich LM. Parameterizations for the cross-sectional area and extinction of cirrus and stratiform ice cloud particles. *J Atmos Sci* 2003;60:936–56.
- [20] Baran AJ. On the scattering and absorption properties of cirrus cloud. *JQSRT* 2004;89:17–36.
- [21] Heymsfield AJ, McFarquhar GM. Mid-latitude and tropical cirrus: microphysical properties. In: Lynch DK, Sassen K, Starr DO'C, Stephens G, editors. *Cirrus*. New York: Oxford University Press, Inc.; 2002. p. 78–101.
- [22] Huang H-L, Yang P, Wei H, Baum BA, Hu Y, Antonelli P, Ackerman SA. Inference of ice cloud properties from high spectral resolution infrared observations. *IEEE Trans Geosci Remote Sens* 2004;42:842–53.
- [23] Baran AJ, Watts PD, Francis PN. Testing the coherence of microphysical and bulk properties retrieved from dual-viewing multispectral satellite radiance measurements. *J Geophys Res* 1999;104:673–88.
- [24] Platt CMR, Dilley AC. Determination of cirrus particle single-scattering phase function from lidar and solar radiometric data. *Appl Opt* 1984;23:380–6.
- [25] Baran AJ, Francis PN. On the radiative properties of cirrus cloud at solar and thermal wavelengths: a test of model consistency using high-resolution airborne radiance measurements. *Q J R Meteorol Soc* 2004;130:763–78.

- [26] Mischenko MI. Light scattering by randomly oriented axially symmetric particles. *J Opt Soc Am* 1991;8:871–82.
- [27] Havemann S, Baran AJ. Extension of T-matrix to scattering of electromagnetic plane waves by non-axisymmetric dielectric particles: application to hexagonal ice cylinders. *JQSRT* 2001;70:139–58.
- [28] Baran AJ, Francis PN, Labonnote L-C, Doutriaux-Boucher M. A scattering phase function for ice cloud: tests of applicability using aircraft and satellite multi-wavelength radiance measurements of cirrus. *Q J R Meteorol Soc* 2001;127:2395–416.
- [29] Fu Q. An accurate parameterization of the solar radiative properties of cirrus clouds for climate models. *J Climate* 1996;9:2058–82.
- [30] Francis PN, Jones A, Saunders RW, Shine KP, Slingo A, Sun Z. An observational and theoretical study of the radiative properties of cirrus: some results from ICE'89. *Quart J Roy Meteor Soc* 1999;120:809–48.
- [31] Heymsfield AJ. Ice particles observed in cirriform cloud at –83C and implications for polar stratospheric clouds. *J Atmos Sci* 1986;43:851–5.
- [32] Lynch DK, Sassen K. Subvisual cirrus. In: Lynch DK, Sassen K, Starr DO'C, Stephens G, editors. *New York: Cirrus Oxford University Press, Inc.; 2002.* p. 256–64.
- [33] Winker DM, Trepte CR. Laminar cirrus observed near the tropical tropopause by LITE. *Geophys Res Lett* 1998;25:3351–4.
- [34] Plass GN, Kattawar GW. Monte Carlo calculations of light scattering by clouds. *Appl Opt* 1968;7:415–9.
- [35] Weinman JA, Davies R. Thermal microwave radiances from horizontally finite clouds of hydrometeors. *J Geophys Res* 1978;83:3099–107.
- [36] Davis JM, Cox SK, McKee T. Vertical and horizontal distributions of solar absorption in finite clouds. *J Atmos Sci* 1979;36:1976–84.
- [37] Harshvardhan J, Weinman A, Davies R. Transport of infrared radiation in cuboidal clouds. *J Atmos Sci* 1981;38:2500–13.
- [38] Stammes K, Tsay S-C, Wiscombe W, Jayaweera K. Numerically stable algorithm for discrete-ordinate-method radiative transfer in multiple scattering and emitting layered media. *Appl Opt* 1988;27:2502–9.
- [39] Collins DG, Blattner WG, Wells MB, Horak HG. Backward Monte Carlo calculations of the polarization characteristics of the radiation emerging from spherical-shell atmospheres. *Appl Opt* 1972;11:2684–705.
- [40] Oikarinen L, Sihvola E, Kyrölä E. Multiple scattering radiance in limb-viewing geometry. *J Geophys Res* 1999;104(D24):261–74.
- [41] Liu Q, Simmer C, Ruprecht E. Three-dimensional radiative transfer effects of clouds in the microwave spectral range. *J Geophys Res* 1996;101(D2):4289–98.
- [42] Davis C, Emde C, Harwood R. A 3D Polarized Reversed Monte Carlo radiative transfer model for mm and sub-mm passive remote sensing in cloudy atmospheres. *IEEE TGARS, MicroRad04 special issue, 2004, in press.*
- [43] Press WH, Teukolsky SA, Vetterling WT, Flannery BP. *NUMERICAL RECIPES in C: the art of scientific computing*, 2nd ed. Cambridge: Cambridge University Press; 1992.
- [44] Marchuk GI, Mikhailov GA, Nazaraliev MA, Darbinjan RA, Kargin BA, Elepov BS. *The Monte Carlo methods in atmospheric optics.* Berlin: Springer; 1980.
- [45] Edwards DP. *GENLN2: a general line-by-line atmospheric transmittance and radiance model/Version 3.0 description and users guide.* National Center for Atmospheric Research, Boulder, Colorado, 1992:NCAR/TN-367+STR.
- [46] Glatthor N, Hoepfner M, Stiller GP, von Clarmann T, Dudhia A, Echle G, Funke B, Hase F. Intercomparison of the KOPRA and the RFM Radiative Transfer codes. *Proceedings of the European Symposium on Atmospheric Measurements for Space, 1999.* p. 757–64.
- [47] A. Dudhia, *The RFM User Manual and Code is available for download at <http://www.atm.ox.ac.uk/RFM>.*
- [48] Kahn BH, Eldering A, Clough SA, Fetzer EJ, Fishbein E, Gunson MR, Lee S-Y, Lester PF, Realmuto VJ. Near micron-sized cirrus cloud particles in high-resolution infrared spectra: an orographic case study. *Geophys Res Lett* 2003;30(8):1441.
- [49] Norton RH, Beer R. New apodizing functions for Fourier spectrometry. *J Opt Soc Am* 1976;66:259–64.
- [50] Remedios JJ. Extreme atmospheric constituent profiles for MIPAS. In: *Proceedings of the European Symposium on Atmospheric Measurements from Space, ESTEC, Netherlands, 20–22 January, vol. 2, 1999.* p. 779–83.
- [51] Matsumoto M, Nishimura T, Mersenne Twister. A 623-dimensionally equidistributed uniform pseudo-random number generator. *ACM Trans Model Comput Simul* 1998;8:3–30.